Voltage Control of Magnetism above Room Temperature in Epitaxial $SrCo_{1-x}Fe_xO_{3-\delta}$

Shuai Ning[1], Qiqi Zhang[2], Connor Occhialini[3], Riccardo Comin[3], Xiaoyan Zhong[2] and Caroline A. Ross[1]**

[1] Department of Materials Science and Engineering, Massachusetts Institute of Technology, Cambridge, Massachusetts 02139, USA.

[2] National Center for Electron Microscopy in Beijing, Key Laboratory of Advanced Materials (MOE), the State Key Laboratory of New Ceramics and Fine Processing, School of Materials Science and Engineering, Tsinghua University, Beijing 100084, People's Republic of China.

[3] Department of Physics, Massachusetts Institute of Technology, Cambridge, MA 02139, USA.

ABSTRACT

Searching for new materials and phenomena to enable voltage control of magnetism and magnetic properties holds compelling interest for the development of low-power non-volatile memory devices. In particular, reversible and non-volatile ON/OFF control of magnetism above room temperature are highly desirable yet still elusive. Here, we report on a non-volatile voltage control of magnetism in epitaxial $SrCo_{1-x}Fe_xO_{3-\delta}$ (SCFO). The substitution of Co with Fe significantly changes the magnetic properties of SCFO. In particular, for the Co/Fe ratio of ~1:1, a switch between nonmagnetic (OFF) and ferromagnetic (ON) state with a Curie temperature above room temperature is accomplished by ionic liquid gating at ambient conditions with voltages

as low as ±2 V, even for films with thickness up to 150 nm. Tuning the oxygen stoichiometry *via* the polarity and duration of gating enables reversible and continuous control of the magnetization between 0 and 100 emu/cm^3 (0.61 μ_B/f.u.) at room temperature. In addition, SCFO was successfully incorporated into self-assembled two-phase vertically aligned nanocomposites, in which the reversible voltage control of magnetism above room temperature is also attained. The notable structural response of SCFO to ionic liquid gating allows remarkable strain couplings between the two oxides in these nanocomposites, with potential for voltage-controlled and strain-mediated functionality based on couplings between structure, composition and physical properties.

KEYWORDS: voltage-controlled magnetism, epitaxial $SrCo_{1-x}Fe_xO_{3-\delta}$, ionic liquid gating, oxygen stoichiometry, self-assembled nanocomposite.

Electrical manipulation of magnetism and magnetic properties is highly desirable both for fundamental science and technological applications. Although advances have been made in current-induced magnetic switching using spin transfer and spin orbit torques,[1,2] voltage control of magnetic properties is attractive as it can further reduce the switching energy by using an electric field instead of a current to accomplish the nonvolatile magnetic reversal.[3] Several processes for voltage control of magnetic properties have been discovered in past decades.[4] One relies on the electric field effect in ferromagnetic (FM) semiconductors or oxides: controlling the carrier density[5,6] or hole doping[7,8] *via* electrostatic gating allows a modification of magnetic properties, but the gating effects are minor and the Curie temperature (T_C) and magnetization of FM semiconductors are very low. This carrier modulation concept has also been demonstrated in FM

metals and alloys,[9,10] but is only limited to ultrathin films and lacks nonvolatility. Beyond this, another strategy for voltage control of magnetism involves the magnetoelectric (ME) coupling in multiferroic systems, including single-phase multiferroics,[11,12] magnet/multiferroic heterostructures,[13,14] and strain-mediated magnetostrictive/piezoelectric composites[15,16] or heterostructures.[17-21] These approaches, however, are limited by the paucity of room-temperature multiferroic materials, as well as the weak ME coupling between magnetic and electric orderings.

Voltage-driven migration of ions in magnetic materials, *i.e.* the magneto-ionic effect, has become an emerging strategy for controlling magnetic properties.[22-34] Utilizing the redox reaction at the interface of an ultra-thin metal or alloy layer adjacent to gate oxides enables a tuning of the magnetic anisotropy,[22-24] coercivity,[25,26] and exchange bias[27] in different systems. An example is provided by O^{2-}-driven easy axis reorientation of a Co/GdO_x heterostructure whose typical response time is of the order of minutes.[22,23] However, this approach is usually limited to metal layer thicknesses of order 1 nm and requires elevated temperatures (>100°C). Although optimizing the gating geometry and the material of gate oxide could realize a faster switching at room temperature, the coercivity has only been tuned by a few oersteds.[26]

In order to accomplish a more robust magnetic response, processes that involve volumetric magnetic phase transitions induced by voltage-driven ion migration have drawn considerable interest.[28-34] Like lithium ions[28,29] that can alter the magnetic properties of bulk-like electrodes (*e.g.* Fe_2O_3) upon charging and discharging in a battery, oxygen[30-33] and hydrogen[30,34] ions are also capable of inducing magnetic phase transitions in certain oxides. Compared with polycrystalline oxide films, *e.g.* Co_3O_4,[32] in which the response is slow even with high voltages, epitaxial complex oxides are of greater interest. This arises from two main reasons: the ordered channels present in the crystal lattice allow easier migrations of oxygen or hydrogen ions; and the strong correlations

among the lattice, spin, charge and orbitals enable a concomitant control of various properties besides magnetic, *e.g.* optical, electrical and thermal.[30,35-38] Many strongly-correlated oxides exhibit fascinating topotactic phase transitions,[30,34,37,39] but obtaining reversible control of the magnetic moment above room temperature in such ordered oxides has remained challenging.

Consider for example the well-studied $SrCoO_{3-\delta}$ system which is described as an oxygen sponge.[40] Varying δ can yield a topotactic phase transition between the fully oxidized ABO_3 (δ≈0) perovskite (P) and oxygen-deficient $A_2B_2O_5$ (δ≈0.5) brownmillerite (BM). The BM phase can be derived notionally from the P structure where oxygen vacancies order in such a way as to form alternating layers of octahedrally and tetrahedrally coordinated *B*-site cations. Ionic liquid (IL) gating, as an emerging method, can not only induce electrostatic effects[6,9,31,41] but can also drive ionic intercalation *via* electrochemical effects,[42-44] which can sufficiently stabilize the P-SCO[30,43] that is difficult to synthesize conventionally due to the unfavorable Co^{+4} valence states and requires annealing in oxygen at extremely high pressures or in ozone. Specifically, the hydrolysis of water absorbed by the IL from the environment can produce oxygen and hydrogen ions upon gating (Figure 1a). Under a negative voltage, the produced oxygen ions will accumulate at the film-ionic-liquid interface and then be forced into the film, decreasing δ and ultimately driving a BM → P transition. Reversing the polarity of gating from negative to positive will then extract oxygen ions, increasing δ and eventually switching the structure back to the oxygen-deficient BM phase. While the P-SCO is ferromagnetic and can show a T_C of 305 K in the ideal crystal,[45] the easy formation of oxygen vacancies drastically weaken the magnetism by lowering the T_C to ~200 K,[46] particularly in the form of thin films. Given that the BM-SCO has a G-type antiferromagnetic ordering with a Néel temperature of 570 K,[47] it is difficult to obtain noticeable magnetic moment change above room-temperature even though IL gating can drive the topotactic phase transition under ambient

conditions (see Figure S1, Supporting Information).[48] Note that gating with higher positive voltage may lead to the intercalation of hydrogen ions into the BM-SCO lattice, yielding a series of hydrogenated-BM phases.[49]

Here, we report on a non-volatile voltage control of magnetic moment above room temperature in epitaxial oxide epitaxial $SrCo_{1-x}Fe_xO_{3-\delta}$ (SCFO) thin films, in which a topotactic phase transition between BM and P structures is also attained similar to that of the end member SCO *via* IL gating. The difference is that substitution of Co with Fe significantly changes the magnetic properties of perovskite phase (P-SCFO). At the optimal Co/Fe ratio, that is ~1/1, we find that the P-SCFO exhibits an enhanced ferromagnetism with a T_C higher than room temperature, which can be suppressed by removing oxygen. IL gating can therefore allow an ON/OFF magnetism transition above room temperature between 100 emu/cm^3 (0.61 μ_B/f.u.) and 0. The magnetic properties are primarily determined by the oxygen stoichiometry (δ) and the ON/OFF switch can be even realized while the material remains in the perovskite structure. Furthermore, we incorporated the magnetically-switchable SCFO into a self-assembled epitaxial 2-phase vertical aligned nanocomposite consisting of pillars of spinel in a P-SCFO matrix, with a similar morphology to that of $BiFeO_3$-$CoFe_2O_4$ (BFO-CFO) nanocomposites.[16] Compared with the minor strain change caused by the piezoelectric effect in conventional multiferroic nanocomposites, the significant structural change of SCFO upon IL gating allows a much greater strain to be induced, which shows potential for voltage-controlled and strain-mediated cross-coupling of properties and offers opportunities for additional applications.

RESULTS AND DISCUSSION

Epitaxial $SrCo_{1-x}Fe_xO_{3-\delta}$ with $x\approx0.5$ thin films with different thickness (30-150 nm) were firstly prepared by pulsed laser deposition (PLD) on 001-oriented $SrTiO_3$ (STO) substrates, and the Co/Fe ratio was measured by X-ray photoelectron spectroscopy (XPS). High-resolution X-ray diffraction (XRD, Figure 1b), reciprocal space mapping (RSM, Figure 1c), and high-angle annular dark-field (HAADF) aberration-corrected scanning transmission electron microscopy (STEM) (Figure 1d) show that the as-grown SCFO ($x\approx0.5$) films exhibit a high-quality BM phase (BM-SCFO).

To provide direct evidence of the IL-gating-induced structure changes, we performed *in situ* XRD measurements on the 60 nm-thick SCFO ($x\approx0.5$) film upon IL gating. It shows that a structural change from BM to P occurs only if the applied negative voltage exceeds −1.5 V (Figure S2b, Supporting Information), meaning that a critical voltage is needed to electrochemically decompose the water and insert oxygen ions into the film. We therefore gated the as-grown BM-SCFO with a voltage of −2 V (denoted as N2G) for 30 mins, and observed a complete transition from BM to the P phase as indicated by the *ex situ* XRD (Figure 1b) and RSM (Figure 1c) analysis, as well as the HAADF and annular bright-field (ABF) STEM images (Figure 1e). In spite of a noticeable out-of-plane contraction due to the infilling of oxygen vacancies, this P phase remains coherently strained to the substrate according to RSM (Figure 1c) as well as STEM (Figure S3, Supporting Information). Chemical mapping reveals a homogeneous distribution of Co and Fe over the entire film thickness (Figure 1f), and atomic-level elemental mappings along both pseudocubic 100- (Figure 1g) and 110- (Figure S3b) zone axes further indicate no specific ordering of Co and Fe ions on the *B*-sites.

If the N2G sample is subsequently gated with positive voltages, the P phase peak shifts towards lower angles (Figure S2c, Supporting Information) as a result of deintercalation of oxygen ions. With a positive voltage up to +3 V, we did not see any signature of hydrogen intercalation. Further

increasing the positive gating voltage could produce hydrogenated phase of SCFO, but that is beyond the scope of the present work. Gating with +2 V (denoted as P2G) for 30 mins almost fully restores the BM phase revealed by *ex situ* XRD (Figure 1b), which is still strained to the substrates according to the RSM (Figure 1c), but the slightly larger q_z of the RSM peak of the P2G sample compared to the as-grown sample suggests a slight residual out-of-plane contraction owing to a small amount of intercalated oxygen ions left in the lattice. The topotactic transitions between BM and P phases are reversible (Figure 1h), and occur much faster in thinner films (*e.g.* 1-minute negative gating can completely drive the BM→ P transition for the 15-nm-thick films). Moreover, these *ex situ* structural characterizations show that the structural transitions are non-volatile (*i.e.* retained after the removal of voltage), as we will describe below for the magnetic transitions.

The chemical states of these two distinct topotactic phases, *i.e.* as-grown BM and N2G-yielded P, were analyzed by X-ray absorption spectroscopy (XAS) at the Co *L*-edge, Fe *L*-edge and O *K*-edge acquired in the total fluorescence yield (TFY) mode. As shown in Figure 1i, both Co and Fe *L*-edge peaks shift towards higher energies after N2G, indicating significant increases in valence states of Co and Fe and a decrease of δ from 0.5 to almost zero as a result of oxygen intercalation. Further support is also provided by the O *K*-edge XAS spectra, particularly the feature *A* in the pre-peak related to Co and Fe 3d bands (green-shaded region), which is ascribed to the strong hybridization of O 2p orbitals with octahedrally coordinated Co and Fe 3d orbitals.[50,51] The substantial enhancement of feature *A* in the N2G sample confirms the presence of the perovskite lattice and indicates a ligand-hole feature that has covalent bond character commonly seen in negative-charge-transfer compounds.[52]

With this understanding of structural transitions and chemical changes, we now turn to the magnetic properties. The as-grown SCFO (x≈0.5), Figure 2a, shows no magnetic remanence or

hysteresis, consistent with the reported antiferromagnetic BM phase.[53] The magnetic measurement was repeated ex situ after 30 mins N2G, and magnetic hysteresis (*M*-*H*) loops are clearly present at room temperature with a saturation magnetization (M_S) of about 100 emu/cm^3 (Figure 2a) and a coercivity of 50 Oe (Figure S4, Supporting Information). Subsequently gating the N2G sample with a voltage of +2 V for 30 mins (P2G) causes the magnetization to completely vanish (Figure 2a). This non-volatile voltage-controlled ON/OFF magnetism is independent of the film thickness up to 150 nm (Figure S5, Supporting Information), and also obtained in samples grown on different substrates, *e.g.* $(LaAlO_3)_{0.3}$-$(SrAl_{0.5}Ta_{0.5}O_3)_{0.7}$ (LSAT) and $LaAlO_3$ (LAO) (Figure S6, Supporting Information), indicating that the hysteretic behavior is an intrinsic and volumetric property of the P-SCFO (x≈0.5). The easy axis of P-SCFO is in-plane, and the anisotropy field is independent of the strain state, implying a negligible magnetoelastic anisotropy contribution. The anisotropy field is ~5 kOe, of which shape anisotropy accounts for $4\pi M_S \approx 1.26$ kOe. This indicates that there is an additional contribution to anisotropy, possibly arising from a growth-induced anisotropy.

To explain the origin of the magnetism of the N2G SCFO, *ex situ* X-ray magnetic circular dichroism (XMCD) at the Co *L*-edge, Fe *L*-edge and O *K*-edge were analyzed in total electron yield (TEY) mode for both the as-grown BM phase and the N2G-yielded P phase. As Figure 2b shows, negligible XMCD signals are seen in the as-grown sample, meaning that the net moment at the Co, Fe and O sites is insignificant, consistent with the magnetometry result. For the N2G sample, clear XMCD signals, *i.e.* the differences between XAS spectra acquired with left and right circularly polarized light, are observed at both Co and Fe *L*-edges. These signals are reversed when the magnetic field is reversed (−*H*), indicating that the nonzero magnetic moments at the Co and Fe sites are ferromagnetically aligned. A weak XMCD signal is also observed at the same position as feature *A* in the O *K*-edge XAS spectra, further confirming that the ferromagnetic coupling is a

result of the strong hybridization of 2p-3d orbitals in P-SCFO. XMCD was also acquired in the TFY mode (Figure S7, Supporting Information), which is consistent with the TEY results.

Along with the reversible ON/OFF magnetism switching, a continuous variation of the room-temperature magnetization can be obtained by varying the gating time. As depicted in Figure 2c, the M_S increases as the duration of N2G increases, showing similar cumulative effects to the resistance variation observed in memristors. Specifically, the M_S increases to ~70 emu/cm^3 after 5 mins N2G, and approaches the maximum of ~100 emu/cm^3 for longer times. For subsequent P2G, the room-temperature M_S is reduced by 80% after as little as 1 min gating, and vanishes after 3 mins gating. The magnetism switching from ON to OFF occurs more rapidly than from OFF to ON, indicating faster oxygen deintercalation from the P phase compared to oxygen intercalation into the BM phase. This might be due to the fact that the tetravalent Co and Fe are unfavorable, which leads to the easier introduction of oxygen vacancies in the P-SCFO.

By alternating the duration and polarity of gating voltage, we can therefore realize multiple-state control of room-temperature magnetization, which is nonvolatile and reversible over multiple cycles. The response time in our work is of the order of a few minutes, which is comparable with that of ultrathin Co/GdO_x stacks[22,23] and much faster than polycrystalline Co_3O_4 films.[32] Response time could be further improved by reducing the dimensions of the film and optimizing the gating geometry, requiring further study.

The Curie temperature T_C of the magnetic SCFO was determined from temperature-dependent magnetization (*M*-*T*) curves. As Figure 2d shows, the FM state turned ON by 30 mins N2G has a T_C of around 340 K, significantly higher than that of P-SCO. Subsequent 1 min P2G lowers the T_C to 300 K and also reduces the total magnetic moment at temperatures below T_C. 3 mins P2G

dramatically suppresses the FM coupling although the lattice still retains the perovskite structure (Figure S8, Supporting Information). This reveals that change in crystal structure from P to BM is not a necessary condition to turn off the FM state, and that the oxygen deficiency plays the crucial role in determining the magnetic properties of P phase. This can be understood in the context of the itinerant-electron model for transition metal oxides.[46,54-56] (Note S9, Supporting Information). We also made a further demonstration of controlling the room-temperature magnetization within the P phase (*i.e.* without a structural transition between BM and P) by initially preparing P-SCFO at higher oxygen pressure. The as-grown P-SCFO is oxygen-deficient and nonmagnetic, while N2G leads to the onset of room-temperature magnetization as the oxygen content in the P phase is increased. (Figure S9, Supporting Information)

To further evaluate the role of composition in the magnetic properties of P-SCFO, we therefore prepared a set of 60 nm-thick SCFO thin films with varying Fe content, x, by combinatorial PLD. N2G induces complete phase transitions from BM to P in all samples, irrespective of x (Figure S10, Supporting Information). Furthermore, the out-of-plane lattice constant of both phases increases with x (Figure 3a-c) due to the larger ionic radius of Fe than isovalent Co.[55]

N2G is able to turn on the magnetic states at room temperature in SCFO thin films of all compositions ($0.32 \leq x \leq 0.76$) (Figure S11, Supporting Information), but the room-temperature M_S depends strongly on x and reaches a maximum at $x \approx 0.5$ (Figure 3d). *M-T* curves (Figure 3e) show that for the Co-rich compositions ($0 < x < 0.5$), T_C and M_S significantly increase with increasing Fe content due to the larger magnetic moment of Fe^{4+} *vs*. Co^{4+}. For the Fe-rich compositions ($0.5 < x < 1$), as x increases the Fe-Fe AFM interactions which compete with the FM coupling,[52] as well as the weakened p-d hybridization due to the larger lattice constant,[54] dramatically diminishes the ferromagnetism. The P-SCFO with $x \approx 0.5$ in our experiments exhibits the greatest magnetic

moment and T_C, providing the best Co/Fe ratio for the objective of controlling magnetism above room temperature.

We next demonstrate the incorporation of SCFO into a self-assembled epitaxial 2-phase oxide nanocomposite by co-deposition from SCO and Fe_3O_4 targets. Nanocomposite oxides exhibit strain-coupling between two co-deposited phases leading to cross-coupled properties such as magnetoelectric behavior not found in the individual phases.[57] The morphology of our nanocomposite (Figure 4a) is akin to the structures seen in multiferroic $BiFeO_3$-$CoFe_2O_4$ (BFO-CFO) nanocomposites[16] where vertical CFO pillars are present within the BFO matrix. The nanocomposite consists of spinel and BM phases (Figure 4b,c), in which spinel pillars are embedded in a BM matrix, and both the spinel and BM are epitaxial with respect to the (001)-oriented STO. Elemental mapping shows that the Fe was preferentially incorporated into the BM phase and the Co into the spinel phase, producing Co_3O_4 spinel pillars within an BM-SCFO matrix (Figure 4d,e). Magnetometry reveals no magnetic moment in the as-grown nanocomposites at room temperature, consistent with the nonmagnetic SCFO matrix and paramagnetic Co_3O_4 pillars (Néel temperature 33 K[58]). IL gating with a voltage of −2 V leads to a phase transition of the SCFO matrix from BM to P (Figure 4b), yielding a ferromagnetic hysteresis loop (Figure 4f) at room temperature. Reversing the gating polarity restores the BM phase and suppresses the magnetism completely. The voltage control of magnetism above room temperature in the nanocomposites is also reversible over multiple cycles and even faster than in monolithic film, which may indicate a role for the spinel in facilitating oxygen migration.

In the IL-gated SCFO-Co_3O_4 nanocomposites, the magnetic signal originates solely from the SCFO phase. However, the Co_3O_4 does itself respond to IL gating as shown by a clear shift of the spinel phase X-ray peak (Figure 4c). This is assumed to be a result of strain transfer from the SCFO

matrix to the spinel pillars when the SCFO transitions between BM and P phases. The imposed strain in the spinel is larger than that produced by the piezoelectric strain in conventional multiferroic nanocomposites such as BFO-CFO consisting of a ferroelectric perovskite and a ferrimagnetic spinel. Our demonstration of an IL-gatable SCFO-Co_3O_4 nanocomposite suggests that SCFO may be coupled with a range of functional oxides, which can offer fascinating opportunities for voltage control of various physical properties based on strain coupling. Furthermore, growth on a (111)-oriented STO substrate is expected to produce SCFO pillars embedded in a continuous spinel matrix.[16] Such a nanocomposite might be appropriate for application as a voltage-controlled magnetic memory.

CONCLUSION

In summary, we have demonstrated non-volatile voltage control of magnetic moment at ambient temperature and pressure in epitaxial SCFO thin films based on the tuning of oxygen stoichiometry *via* IL gating. At a Co/Fe ratio of ~1:1, ferromagnetism with a T_C above room temperature and RT M_S of 100 emu/cm^3 (0.61 μ_B/f.u.) is obtained in the perovskite phase of SCFO. Extracting oxygen from the perovskite SCFO with a low positive voltage applied during IL gating decreases T_C and the magnetic moment while maintaining the P phase structure; longer gating duration completely suppresses the ferromagnetic ordering and ultimately produces the nonmagnetic brownmillerite phase. Reinserting oxygen by gating with a positive voltage recovers the ferromagnetic state, thus enabling a reversible ON/OFF control of the magnetic moment above room temperature just by alternating the polarity of the gating voltage. The dependence of the magnetic moment of perovskite SCFO on the oxygen deficiency enables continuous variation of the magnetization by regulating the duration of gating. In addition, varying the Co/Fe ratio significantly modifies the

magnetic properties of P-SCFO, allowing a tuning of the ON/OFF magnetism switching temperature. Furthermore, we incorporated the SCFO into self-assembled two-phase oxide nanocomposites consisting of SCFO and a spinel phase. Gating the SCFO not only modulated its magnetic moment, but also led to a large strain transfer into the spinel phase due to the structural response of the SCFO. These results reveal the potential for voltage-controlled phenomena associated with the coupling between structure, composition and physical properties.

EXPERIMENTAL SECTION

Thin film preparation. The monolithic $SrCo_{1-x}Fe_xO_{3-\delta}$ thin films were prepared by pulsed laser deposition using a KrF excimer laser (λ=248 nm) with 1.3 J/cm^2 fluence and 5 Hz repetition rate. $SrCoO_{3-\delta}$ and $SrFeO_{3-\delta}$ targets were ablated alternately for 60 shots each, so that each "layer" deposited from the targets is less than a monolayer thick. The growth temperature was 850 °C and the oxygen partial pressure, $p(O_2)$, was 0.1 mTorr. After growth, the films were cooled down to room temperature in the same $p(O_2)$ at a rate of 20 °C/min. Details of the combinatorial growth are discussed in the Note S11 in Supporting Information. The self-assembled nanocomposites were prepared by alternately ablating $SrCoO_{3-\delta}$ and Fe_3O_4 targets for 80 and 40 shots respectively, using the same laser conditions with growth temperature of 850 °C and $p(O_2)$ = 20 mTorr.

Ionic Liquid gating experiments. Ionic liquid gating experiments were performed with 1-hexyl-3-methylimidazolium bis(trifluormethylsulfonyl)imide (HMIM-TFSI) as the electrolyte (Sigma-Aldrich, USA). The SCFO thin films or self-assembled nanocomposites were immersed in the ionic liquid with a spiral Pt wire as counter electrode, and another Pt probe was spring loaded to directly contact the sample surface. A Hewlett Packard 6632A Power Supply was used to apply the gating voltage.

Structure and composition characterizations. The crystalline structure was characterized by both XRD and RSM using a Rigaku SmartLab high-resolution diffractometer with Cu $K\alpha_1$ radiation (λ=1.5406 Å) as X-ray source and an incident beam Ge-(220) double-bounce monochromator. *In situ* XRD measurements upon IL gating were also performed using the same diffractometer at ambient conditions with the home-made IL gating setup mounted on the sample stage. The chemical composition is estimated by using a Thermo Scientific K-Alpha+ XPS system with Al $K\alpha$ (1486.6 eV) as the X-ray source. Before collecting the data, the sample surface was cleaned with a cluster ion beam for 30 seconds.

XAS and XMCD measurements. XAS and XMCD measurements at Co *L*-edges, Fe *L*-edges and O *K*-edges were carried out in both total electron yield (TEY) and total fluorescence yield (TFY) modes using the beamline 4-ID-C of the Advanced Photon Source at Argonne National Laboratory. The temperature was set to 200 K to obtain a good signal to noise ratio. The magnetic field (0.5 T) was applied during the measurements by means of an octupole magnet along the beam incident direction with the incident angle of 25° from the normal of the sample plane. XAS curves shown in Figure 1 are the average of left and right circular. Reference scans of elemental Fe measured in TEY simultaneously indicate negligible energy shift throughout the experiments.

Magnetic properties characterization. The magnetic hysteresis loops were measured using a Digital Measurement System 7035B vibrating sample magnetometer (VSM) at room temperature. The temperature-dependent magnetization measurements, including both field cooling (FC) and zero field cooling (ZFC), were carried out using a Quantum Design MPMS-3 SQUID magnetometer with the magnetic field (1.3 T) applied along the in-plane direction of the film.

TEM imaging and chemical mapping. The cross-sectional samples of monolithic SCFO thin films along the $<100>_o$ and $<110>_o$ zone axes for TEM experiments were prepared through Zeiss

Auriga Focused Ion Beam (FIB), and fine ion-milled with argon ion milling to remove the amorphous layer. High-resolution image and spectrum experiments were performed with an aberration-corrected STEM FEI Titan Cubed Themis with a field emission gun, and operated at 300 kV. The STEM images were detected with a camera length of 115 mm through a HAADF detector whose collection semi-angle range is 48-200 mrad, and a dark field 4 detector for ABF images whose collection semi-angle range is 12-48 mrad. The EELS were collected with a camera length of 36 mm through a Gatan Image Filter system (Gatan Quantum 965 Spectrometer), and the range of energy loss spectrum we acquired is 450-900 eV. The cross-sectional TEM specimens of the nanocomposites were prepared using a Helios Nanolab 600 Dual Beam Focused Ion Beam (FIB) Milling System. The high-resolution TEM images and STEM-EDS mapping on the nanocomposites were collected with a JEOL 2010 FEG Analytical Electron Microscope at 200 kV.

ASSOCIATED CONTENT

Supporting Information.

The following files are available free of charge *via* the Internet at http://pubs.acs.org.

Magnetism of both BM and P phases of SCO and SFO; Structural evolution of SCFO (x≈0.5) with IL gating; STEM images of as-grown and N2G SCFO (x≈0.5); RT in-plane coercivity and remanence of 60 nm-thick SCFO (x≈0.5); Magnetism of P-SCFO (x≈0.5) thin films with different thickness; Structural and magnetic transitions in SCFO (x≈0.5) on different substrates; TFY XMCD analysis; Structural evolution of SCFO (x≈0.5) with the duration of P2G; Dependence of FM properties on oxygen deficiency in P-SCFO; Magnetism switching without topotactic phase transitions; Combinatorial growth of SCFO thin films with varying x (PDF)

AUTHOR INFORMATION

Corresponding Author

*E-mail: sning@mit.edu, *E-mail: caross@mit.edu

Author Contributions

S.N. conceived and designed the experiments. C.R. supervised the project. S.N. prepared the samples, and carried out the ionic liquid gating experiments, and conducted the characterization on the crystal structure, chemical composition and magnetic properties. Q.Z. performed the STEM imaging and chemical mapping analysis on the monolithic SCFO thin films under the supervision of X.Z. C.O. carried out the XAS and XMCD measurements under the supervision of R.C. S.N. and C.R. wrote the manuscript. All authors discussed the results and contributed to the manuscript.

ACKNOWLEDGMENT

The authors thank Dr. Yong Zhang for his help regarding the elemental mapping on the nanocomposites and Dr. Charles Settens for his help on XRD measurements. The authors are grateful to Dr. Richard Rosenberg, Dr. Jonathan Pelliciari, Jackson Bauer and Ethan Rosenberg for their help on XAS and XMCD measurements, to Prof. Jing Zhu for helpful aids and to Prof. Lei Bi for helpful discussions. This work was supported by NSF under award DMR-1419807, and shared experimental facilities of the MIT MRSEC through the MRSEC Program of the National Science Foundation under award DMR-1419807 were used. This work made use of the resources of the National Center for Electron Microscopy in Beijing. This work also used resources of the Advanced Photon Source, a U.S. Department of Energy (DOE) Office of Science User Facility operated for the DOE Office of Science by Argonne National Laboratory under Contact No. DE-AC02-06CH11357. Q.Z. and X.Z thanks for the financial supports by National Key Research and

Development Program (2016YFB0700402), National Natural Science Foundation of China (11834009, 51761135131, 51822105, 51671112, 51788104) and School of Materials Science and Engineering at Tsinghua University.

REFERENCES

(1) Brataas, A.; Kent, A. D.; Ohno, H. Current-Induced Torques in Magnetic Materials. *Nat. Mater.* **2012,** *11*, 372-381.

(2) Železný, J.; Wadley, P.; Olejník, K.; Hoffmann, A.; Ohno, H. Spin Transport and Spin Torque in Antiferromagnetic Devices. *Nat. Phys.* **2018,** *14*, 220-228.

(3) Matsukura, F.; Tokura, Y.; Ohno, H. Control of Magnetism by Electric Fields. *Nat. Nanotechnol.* **2015,** *10*, 209-220.

(4) Song, C.; Cui, B.; Li, F.; Zhou, X. J.; Pan, F. Recent Progress in Voltage Control of Magnetism: Materials, Mechanisms, and Performance. *Prog Mater Sci* **2017,** *87*, 33-82.

(5) Ohno, H.; Chiba, D.; Matsukura, F.; Omiya, T.; Abe, E.; Dietl, T.; Ohno, Y.; Ohtani, K. Electric-Field Control of Ferromagnetism. *Nature* **2000,** *408*, 944-946.

(6) Yamada, Y.; Ueno, K.; Fukumura, T.; Yuan, H. T.; Shimotani, H.; Iwasa, Y.; Gu, L.; Tsukimoto, S.; Ikuhara, Y.; Kawasaki, M. Electrically Induced Ferromagnetism at Room Temperature in Cobalt-Doped Titanium Dioxide. *Science* **2011,** *332*, 1065-1067.

(7) Walter, J.; Wang, H.; Luo, B.; Frisbie, C. D.; Leighton, C. Electrostatic versus Electrochemical Doping and Control of Ferromagnetism in Ion-Gel-Gated Ultrathin $La_{0.5}Sr_{0.5}CoO_{3-\delta}$. *ACS Nano* **2016,** *10*, 7799-7810.

(8) Walter, J.; Charlton, T.; Ambaye, H.; Fitzsimmons, M. R.; Orth, P. P.; Fernandes, R. M.; Leighton, C. Giant Electrostatic Modification of Magnetism *via* Electrolyte-Gate-Induced Cluster Percolation in $La_{1-x}Sr_xCoO_{3-\delta}$. *Phys. Rev. Materials* **2018,** *2*, 111406.

(9) Weisheit, M.; Fahler, S.; Marty, A.; Souche, Y.; Poinsignon, C.; Givord, D. Electric Field-Induced Modification of Magnetism in Thin-Film Ferromagnets. *Science* **2007,** *315*, 349-351.

(10) Shiota, Y.; Nozaki, T.; Bonell, F.; Murakami, S.; Shinjo, T.; Suzuki, Y. Induction of Coherent Magnetization Switching in a Few Atomic Layers of FeCo Using Voltage Pulses. *Nat. Mater.* **2011,** *11*, 39-43.

(11) Wang, J.; Neaton, J. B.; Zheng, H.; Nagarajan, V.; Ogale, S. B.; Liu, B.; Viehland, D.; Vaithyanathan, V.; Schlom, D. G.; Waghmare, U. V.; Spaldin, N. A.; Rabe, K. M.; Wuttig, M.; Ramesh, R. Epitaxial $BiFeO_3$ Multiferroic Thin Film Heterostructures. *Science* **2003,** *299*, 1719-1722.

(12) Tokunaga, Y.; Iguchi, S.; Arima, T.; Tokura, Y. Magnetic-Field-Induced Ferroelectric State in $DyFeO_3$. *Phys. Rev. Lett.* **2008,** *101*, 097205.

(13) Chu, Y. H.; Martin, L. W.; Holcomb, M. B.; Gajek, M.; Han, S. J.; He, Q.; Balke, N.; Yang, C. H.; Lee, D.; Hu, W.; Zhan, Q.; Yang, P. L.; Fraile-Rodriguez, A.; Scholl, A.; Wang, S. X.; Ramesh, R. Electric-Field Control of Local Ferromagnetism Using a Magnetoelectric Multiferroic. *Nat. Mater.* **2008,** *7*, 478-482.

(14) Heron, J. T.; Trassin, M.; Ashraf, K.; Gajek, M.; He, Q.; Yang, S. Y.; Nikonov, D. E.; Chu, Y. H.; Salahuddin, S.; Ramesh, R. Electric-Field-Induced Magnetization Reversal in a Ferromagnet-Multiferroic Heterostructure. *Phys. Rev. Lett.* **2011,** *107*, 217202.

(15) Zheng, H.; Wang, J.; Lofland, S. E.; Ma, Z.; Mohaddes-Ardabili, L.; Zhao, T.; Salamanca-Riba, L.; Shinde, S. R.; Ogale, S. B.; Bai, F.; Viehland, D.; Jia, Y.; Schlom, D. G.; Wuttig, M.;

Roytburd, A.; Ramesh, R. Multiferroic $BaTiO_3$-$CoFe_2O_4$ Nanostructures. *Science* **2004,** *303*, 661-663.

(16) Zheng, H.; Straub, F.; Zhan, Q.; Yang, P. L.; Hsieh, W. K.; Zavaliche, F.; Chu, Y. H.; Dahmen, U.; Ramesh, R. Self-Assembled Growth of $BiFeO_3$–$CoFe_2O_4$ Nanostructures. *Adv. Mater.* **2006,** *18*, 2747-2752.

(17) Eerenstein, W.; Wiora, M.; Prieto, J. L.; Scott, J. F.; Mathur, N. D. Giant Sharp and Persistent Converse Magnetoelectric Effects in Multiferroic Epitaxial Heterostructures. *Nat. Mater.* **2007,** *6*, 348-351.

(18) Sahoo, S.; Polisetty, S.; Duan, C.-G.; Jaswal, S. S.; Tsymbal, E. Y.; Binek, C. Ferroelectric Control of Magnetism in $BaTiO_3$/Fe Heterostructures *via* Interface Strain Coupling. *Phys. Rev. B* **2007,** *76*, 092108.

(19) Kim, H. K.; Schelhas, L. T.; Keller, S.; Hockel, J. L.; Tolbert, S. H.; Carman, G. P. Magnetoelectric Control of Superparamagnetism. *Nano Lett.* **2013,** *13*, 884-888.

(20) Cherifi, R. O.; Ivanovskaya, V.; Phillips, L. C.; Zobelli, A.; Infante, I. C.; Jacquet, E.; Garcia, V.; Fusil, S.; Briddon, P. R.; Guiblin, N.; Mougin, A.; Unal, A. A.; Kronast, F.; Valencia, S.; Dkhil, B.; Barthelemy, A.; Bibes, M. Electric-Field Control of Magnetic Order above Room Temperature. *Nat. Mater.* **2014,** *13*, 345-351.

(21) Yan, H. *et al.* A Piezoelectric, Strain-Controlled Antiferromagnetic Memory Insensitive to Magnetic Fields. *Nat. Nanotechnol.* **2019,** *14*, 131-136.

(22) Bi, C.; Liu, Y.; Newhouse-Illige, T.; Xu, M.; Rosales, M.; Freeland, J. W.; Mryasov, O.; Zhang, S.; te Velthuis, S. G.; Wang, W. G. Reversible Control of Co Magnetism by Voltage-Induced Oxidation. *Phys. Rev. Lett.* **2014,** *113*, 267202.

(23) Bauer, U.; Yao, L.; Tan, A. J.; Agrawal, P.; Emori, S.; Tuller, H. L.; van Dijken, S.; Beach, G. S. Magneto-Ionic Control of Interfacial Magnetism. *Nat. Mater.* **2015,** *14*, 174-181.

(24) Tan, A. J.; Huang, M.; Avci, C. O.; Buttner, F.; Mann, M.; Hu, W.; Mazzoli, C.; Wilkins, S.; Tuller, H. L.; Beach, G. S. D. Magneto-Ionic Control of Magnetism Using a Solid-State Proton Pump. *Nat. Mater.* **2019,** *18*, 35-41.

(25) Gilbert, D. A.; Grutter, A. J.; Arenholz, E.; Liu, K.; Kirby, B. J.; Borchers, J. A.; Maranville, B. B. Structural and Magnetic Depth Profiles of Magneto-Ionic Heterostructures beyond the Interface Limit. *Nat. Commun.* **2016,** *7*, 12264.

(26) Li, H. B.; Lu, N.; Zhang, Q.; Wang, Y.; Feng, D.; Chen, T.; Yang, S.; Duan, Z.; Li, Z.; Shi, Y.; Wang, W.; Wang, W. H.; Jin, K.; Liu, H.; Ma, J.; Gu, L.; Nan, C.; Yu, P. Electric-Field Control of Ferromagnetism through Oxygen Ion Gating. *Nat. Commun.* **2017,** *8*, 2156.

(27) Gilbert, D. A.; Olamit, J.; Dumas, R. K.; Kirby, B. J.; Grutter, A. J.; Maranville, B. B.; Arenholz, E.; Borchers, J. A.; Liu, K. Controllable Positive Exchange Bias *via* Redox-Driven Oxygen Migration. *Nat. Commun.* **2016,** *7*, 11050.

(28) Dasgupta, S.; Das, B.; Knapp, M.; Brand, R. A.; Ehrenberg, H.; Kruk, R.; Hahn, H. Intercalation-Driven Reversible Control of Magnetism in Bulk Ferromagnets. *Adv. Mater.* **2014,** *26*, 4639-4644.

(29) Zhang, Q.; Luo, X.; Wang, L.; Zhang, L.; Khalid, B.; Gong, J.; Wu, H. Lithium-Ion Battery Cycling for Magnetism Control. *Nano Lett.* **2016,** *16*, 583-587.

(30) Lu, N. *et al.* Electric-Field Control of Tri-State Phase Transformation with a Selective Dual-Ion Switch. *Nature* **2017,** *546*, 124-128.

(31) Molinari, A.; Hahn, H.; Kruk, R. Voltage-Controlled On/Off Switching of Ferromagnetism in Manganite Supercapacitors. *Adv. Mater.* **2018,** *30*, 1703908.

(32) Quintana, A.; Menendez, E.; Liedke, M. O.; Butterling, M.; Wagner, A.; Sireus, V.; Torruella, P.; Estrade, S.; Peiro, F.; Dendooven, J.; Detavernier, C.; Murray, P. D.; Gilbert, D. A.; Liu, K.; Pellicer, E.; Nogues, J.; Sort, J. Voltage-Controlled On-Off Ferromagnetism at Room Temperature in a Single Metal Oxide Film. *ACS Nano* **2018,** *12*, 10291-10300.

(33) Cui, B.; Song, C.; Li, F.; Zhong, X. Y.; Wang, Z. C.; Werner, P.; Gu, Y. D.; Wu, H. Q.; Saleem, M. S.; Parkin, S. S. P.; Pan, F. Electric-Field Control of Oxygen Vacancies and Magnetic Phase Transition in a Cobaltite/Manganite Bilayer. *Phys. Rev. Applied* **2017,** *8*.

(34) Wang, M. *et al.* Manipulate the Electronic and Magnetic States in $NiCo_2O_4$ Films through Electric-Field-Induced Protonation at Elevated Temperature. *Adv. Mater.* **2019**, e1900458.

(35) Lu, Q.; Huberman, S.; Zhang, H.; Song, Q.; Wang, J.; Vardar, G.; Hunt, A.; Waluyo, I.; Chen, G.; Yildiz, B. Bi-Directional Tuning of Thermal Transport in $SrCoO_x$ with Electrochemically Induced Phase Transitions. *Nat. Mater.* **2020**, 19, 655-662.

(36) Ning, S.; Huberman, S. C.; Ding, Z.; Nahm, H.-H.; Kim, Y.-H.; Kim, H.-S.; Chen, G.; Ross, C. A. Anomalous Defect Dependence of Thermal Conductivity in Epitaxial WO_3 Thin Films. *Adv. Mater.* **2019,** *31*, 1903738.

(37) Yi, D.; Wang, Y.; van 't Erve, O. M. J.; Xu, L.; Yuan, H.; Veit, M. J.; Balakrishnan, P. P.; Choi, Y.; N'Diaye, A. T.; Shafer, P.; Arenholz, E.; Grutter, A.; Xu, H.; Yu, P.; Jonker, B. T.; Suzuki, Y. Emergent Electric Field Control of Phase Transformation in Oxide Superlattices. *Nat. Commun.* **2020,** *11*, 902.

(38) Jeong, J.; Aetukuri, N.; Graf, T.; Schladt, T. D.; Samant, M. G.; Parkin, S. S. Suppression of Metal-Insulator Transition in VO_2 by Electric Field-Induced Oxygen Vacancy Formation. *Science* **2013,** *339*, 1402-1405.

(39) Saleem, M. S.; Cui, B.; Song, C.; Sun, Y.; Gu, Y.; Zhang, R.; Fayaz, M. U.; Zhou, X.; Werner, P.; Parkin, S. S. P.; Pan, F. Electric Field Control of Phase Transition and Tunable Resistive Switching in $SrFeO_{2.5}$. *ACS Appl Mater Interfaces* **2019,** *11*, 6581-6588.

(40) Jeen, H.; Choi, W. S.; Biegalski, M. D.; Folkman, C. M.; Tung, I. C.; Fong, D. D.; Freeland, J. W.; Shin, D.; Ohta, H.; Chisholm, M. F.; Lee, H. N. Reversible Redox Reactions in an Epitaxially Stabilized $SrCoO_x$ Oxygen Sponge. *Nat. Mater.* **2013,** *12*, 1057-1063.

(41) Ueno, K.; Nakamura, S.; Shimotani, H.; Ohtomo, A.; Kimura, N.; Nojima, T.; Aoki, H.; Iwasa, Y.; Kawasaki, M. Electric-Field-Induced Superconductivity in an Insulator. *Nat. Mater.* **2008,** *7*, 855-858.

(42) Leighton, C. Electrolyte-Based Ionic Control of Functional Oxides. *Nat. Mater.* **2019,** *18*, 13-18.

(43) Cui, B.; Werner, P.; Ma, T.; Zhong, X.; Wang, Z.; Taylor, J. M.; Zhuang, Y.; Parkin, S. S. P. Direct Imaging of Structural Changes Induced by Ionic Liquid Gating Leading to Engineered Three-Dimensional Meso-Structures. *Nat. Commun.* **2018,** *9*, 3055.

(44) Yuan, H.; Shimotani, H.; Ye, J.; Yoon, S.; Aliah, H.; Tsukazaki, A.; Kawasaki, M.; Iwasa, Y. Electrostatic and Electrochemical Nature of Liquid-Gated Electric-Double-Layer Transistors Based on Oxide Semiconductors. *J. Am. Chem. Soc.* **2010,** *132*, 18402-18407.

(45) Long, Y.; Kaneko, Y.; Ishiwata, S.; Taguchi, Y.; Tokura, Y. Synthesis of Cubic $SrCoO_3$ Single Crystal and Its Anisotropic Magnetic and Transport Properties. *J Phys Condens Matter* **2011,** *23*, 245601.

(46) Taguchi, H.; Shimada, M.; Koizumi, M. The effect of Oxygen Vacancy on the Magnetic Properties in the System $SrCoO_{3-\delta}$ ($0 < \delta < 0.5$). *J. Solid State Chem.* **1979,** *29*, 221-225.

(47) Takeda, T.; Yamaguchi, Y.; Watanabe, H. Magnetic Structure of $SrCoO_{2.5}$. *J. Phys. Soc. Jpn.* **1972,** *33*, 970-972.

(48) Wang, D.; Meng, L.; Wei, L.; Shi, P.; Chen, Y.; Yan, S.; Tian, Y.; Liu, G.; Mei, L. Reversible Phase Switching between Antiferromagnetic $SrCoO_{2.5}$ and Ferromagnetic $SrCoO_{3-\delta}$ by a Flexible Solid-State Electrolyte Gate. *J. Magn. Magn. Mater.* **2020,** *496*, 165926.

(49) Li, H. B. *et al.* Electric Field–Controlled Multistep Proton Evolution in $H_xSrCoO_{2.5}$ with Formation of H–H Dimer. *Adv. Sci.* **2019**, 1901432.

(50) Karvonen, L.; Valkeapää, M.; Liu, R.-S.; Chen, J.-M.; Yamauchi, H.; Karppinen, M. O-Kand Co-LXANES Study on Oxygen Intercalation in Perovskite $SrCoO_{3-\delta}$. *Chem. Mater.* **2010,** *22*, 70-76.

(51) Galakhov, V. R.; Kurmaev, E. Z.; Kuepper, K.; Neumann, M.; McLeod, J. A.; Moewes, A.; Leonidov, I. A.; Kozhevnikov, V. L. Valence Band Structure and X-ray Spectra of Oxygen-Deficient Ferrites $SrFeO_x$. *J. Phys. Chem. C* **2010,** *114*, 5154-5159.

(52) Abbate, M.; Zampieri, G.; Okamoto, J.; Fujimori, A.; Kawasaki, S.; Takano, M. X-Ray Absorption of the Negative Charge-Transfer Material $SrFe_{1-x}Co_xO_3$. *Phys. Rev. B* **2002,** *65*, 165120.

(53) Battle, P. D.; Gibb, T. C.; Lightfoot, P. The Crystal and Magnetic Structures of Sr_2CoFeO_5. *J. Solid State Chem.* **1988,** *76*, 334-339.

(54) Lim, J.; Yu, J. Role of Oxygen Vacancy in the Spin-State Change and Magnetic Ordering in $SrCoO_{3-\delta}$. *Phys. Rev. B* **2018,** *98*, 085106.

(55) Takeda, T.; Watanabe, H. Magnetic Properties of the System $SrCo_{1-x}Fe_xO_{3-y}$. *J. Phys. Soc. Jpn.* **1972,** *33*, 973-978.

(56) Takeda, T.; Yamaguchi, Y.; Watanabe, H. Magnetic Structure of $SrFeO_3$. *J. Phys. Soc. Jpn.* **1972,** *33*, 967-969.

(57) MacManus-Driscoll, J. L. Self-Assembled Heteroepitaxial Oxide Nanocomposite Thin Film Structures: Designing Interface-Induced Functionality in Electronic Materials. *Adv. Funct. Mater.* **2010,** *20*, 2035-2045.

(58) Kündig, W.; Kobelt, M.; Appel, H.; Constabaris, G.; Lindquist, R. H. Mössbauer Studies of Co_3O_4; Bulk Material and Ultrafine Particles. *J. Phys. Chem. Solids* **1969,** *30*, 819-826.

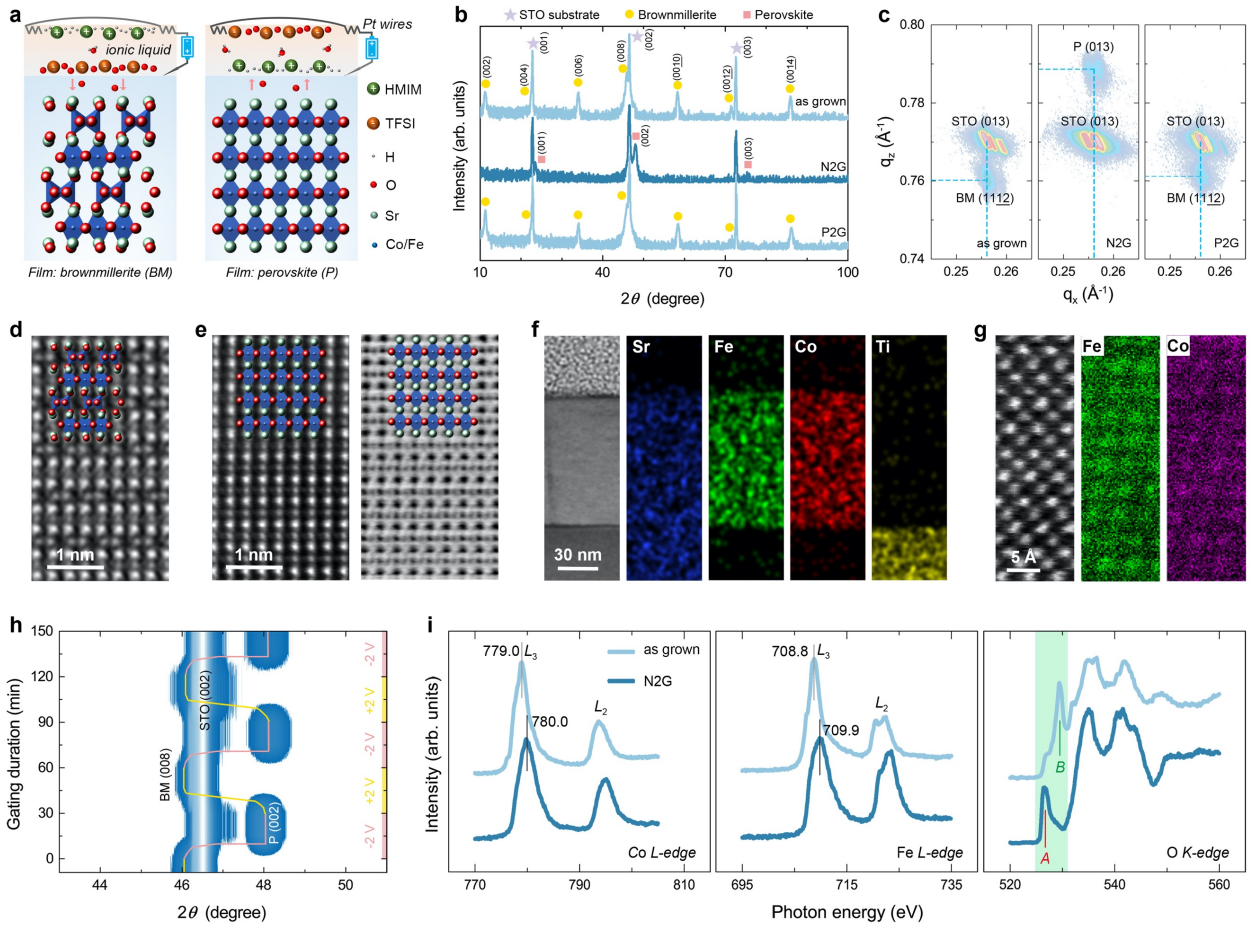

Figure 1. Voltage-controlled phase transitions in $SrCo_{0.5}Fe_{0.5}O_{3-\delta}$ by ionic liquid gating. (a), schematic of ionic liquid gating with negative and positive voltages. (b, c), *ex situ* high-resolution XRD (b) and *ex situ* RSM around the (013) peaks of STO (c) on the as-grown, -2 V gated (N2G) and +2 V gated (P2G) 60 nm-thick SCFO (x≈0.5) film. (d), HAADF-STEM image of as-grown BM sample taken with the zone axis along the orthorhombic $[100]_o$ direction (pseudocubic [110] direction). (e), HAADF (left) and the ABF (right) images of the P phase of N2G sample with zone axis along the pseudocubic [110] direction. (f, g), elemental mapping of the N2G sample by energy-dispersive x-ray spectroscopy (EDS) (f) and electron energy-loss spectroscopy (EELS) (g). (h), *in situ* XRD measurements around the STO (002) peak collected with the gating voltage alternated between -2 V and +2 V on the 60 nm-thick SCFO (x≈0.5). (i), *ex situ* XAS spectra of cobalt *L*-edges, iron *L*-edges and oxygen *K*-edges for as-grown and N2G 60 nm-thick SCFO (x≈0.5) thin films. Shaded region in oxygen *K*-edges spectra is related to the Co and Fe 3d bands. The feature *A* is ascribed to Co and Fe ions with oxygen octahedral coordination geometry while the feature *B* relates to superoxide species mostly in the surface regions.

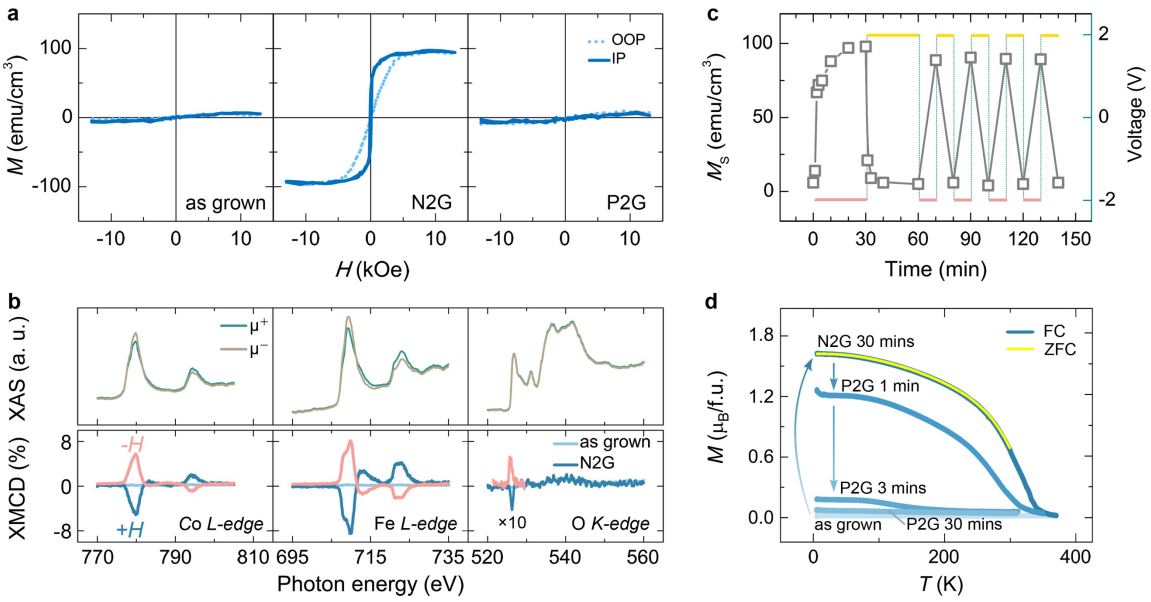

Figure 2. Voltage control of magnetism in $SrCo_{0.5}Fe_{0.5}O_{3-\delta}$. (a), RT *M*-*H* loops of the as-grown, N2G, and P2G 60 nm-thick SCFO (x≈0.5) thin films on STO substrates. (b), TEY XMCD spectra (lower panel) at Co *L*-edges, Fe *L*-edges and O *K*-edges of both as-grown and N2G samples, *i.e.* the differences of two XAS spectra taken with left (μ^+) and right (μ^-) circularly polarized light (example of the N2G sample is shown in the upper panel). During the measurements, the magnetic field (0.5 T) was applied parallel (+*H*) to the incident direction of the X-ray which is at 25° from the normal of film surface. Reversing the magnetic field (−*H*) led to simultaneous flip of the XMCD signals at all Co, Fe and O sites. (c), evolution of the RT M_S of SCFO (x≈0.5) thin films with the polarity and duration of ionic liquid gating. (d), *ex situ* field cooling (FC) *M*-*T* curves of the as-grown SCFO (x≈0.5), that after 30 mins N2G, and that after 1 min, 3 mins and 30 mins P2G measured in a sequence and with the magnetic field (1.3 T) parallel to the film plane. the Zero field cooling (ZFC) *M*-*T* curve of 30 mins N2G sample is also measured.

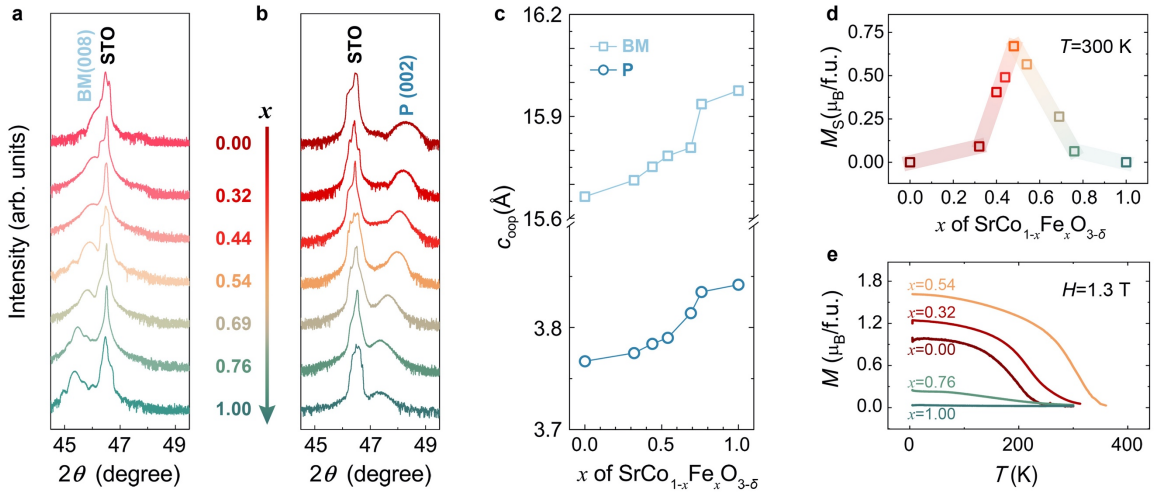

Figure 3. Dependence of structural and magnetic properties of SCFO thin films on Fe content. (a, b), high-resolution XRD patterns of as-grown (a) and N2G (b) SCFO thin films on STO with varying *x*. (c), the dependence of out-of-plane lattice constants on *x* for both the as-grown and N2G samples with the analysis of XRD shown in (a) and (b). (d, e), the dependence of the RT M_S (d) and the *M*-*T* curves (measured with a field of 1.3 T parallel to the film plane) (e) on the Fe content in the P-SCFO yielded by 30 mins N2G.

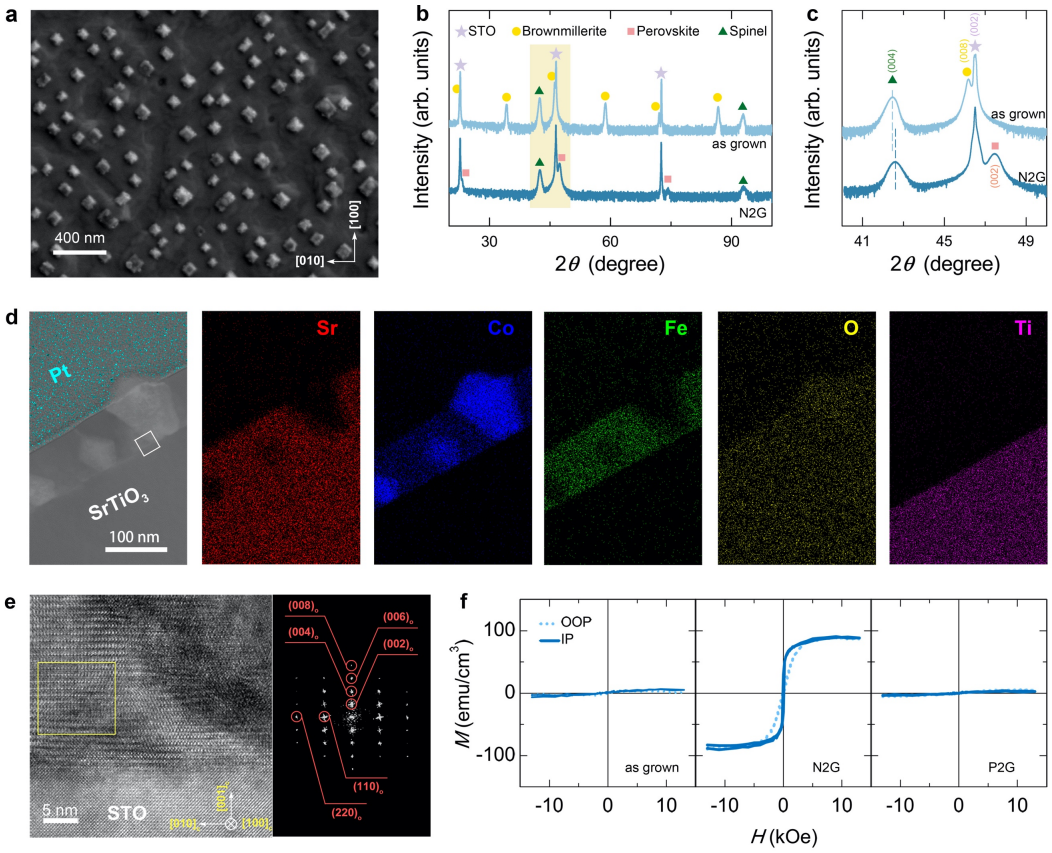

Figure 4. Magnetism switching and strain coupling in self-assembled nanocomposites. (a), scanning electron microscopy (SEM) image of the nanocomposites grown on the 001-oriented STO substrate. (b, c), the high-resolution XRD patterns of as-grown nanocomposite and that after 30 mins N2G in a full range (b) and around the (002) peaks of the STO (c). (d), elemental mapping on the cross-sectional TEM specimen of the nanocomposite. (e), high-resolution TEM image of the interfacial region outlined in (d), and a fast Fourier transform (FFT) image taken at the matrix region outlined by yellow rectangle which reveals a characteristic electron diffraction pattern of the orthorhombic brownmillerite structure. (f), RT *M*-*H* loops of the as-grown, N2G, and P2G nanocomposites and the M_S is normalized by the entire volume of the nanocomposites.

ToC figure

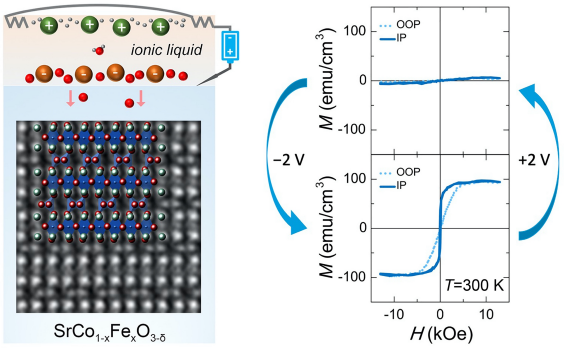
ionic liquid
SrCo1-xFexO3-δ
−2 V
+2 V
OOP
IP
M (emu/cm3)
100
0
-100
T=300 K
-10
0
10
H (kOe)